Temperature effects on elastic constants and related properties of apatites

Aritri Roy [a], Bikash Kanungo [b], Puneet Kumar Patra [c], Baidurya Bhattacharya [d],*

[a] *Advanced Technology Development Centre, Indian Institute of Technology Kharagpur, West Bengal 721302, India*
[b] *Department of Mechanical Engineering, University of Michigan, Ann Arbor, MI 48109, United States*
[c] *Department of Civil Engineering, Indian Institute of Technology Kharagpur, West Bengal 721302, India*
[d] *Civil and Environmental Engineering, University of Delaware, Newark, DE, United States*

A B S T R A C T

The application of apatites, a class of naturally occurring calcium phosphate minerals with the most common forms being hydroxyapatite (HAP), fluorapatite (FAP) and chlorapatite (ClAP), range from primary production of phosphorus, to bone and dental implants, to potential usage in carbon sequestration and nuclear waste immobilization including those that involve exposure to high temperatures. Due to their hexagonal structure, apatites have five independent elastic constants: nevertheless, experimental studies commonly report isotropic properties, and limited computational results available in the literature exhibit a large scatter. Moreover, investigation of temperature dependence of apatite elastic properties which would be essential for designing future applications is yet to be addressed in the current state of the art. In this work, we evaluate the single crystal elastic constants of the three apatite structures using stress–strain relationships: first from density functional theory (DFT) using ultrasoft pseudopotential with PBEsol exchange–correlation functional under generalized gradient approximation (GGA) on a single unit cell , and then with molecular dynamics (MD) with a 5×5×5 unit cell using a core–shell based potential model at temperatures varying from 10K to 1500K. In this temperature range, apatites exhibit the highest stiffness along the 'c' axis, and their elastic constants noticeably decrease with increasing temperature. At very high temperatures, C_{33} becomes greater than C_{11} for both FAP and ClAP. It is noteworthy that our DFT study exhibits better conformity with experimental findings when compared to other DFT studies reported in literature. Additionally, MD studies have demonstrated favorable consistency in predicting elastic constants, potentially as a result of fitting potential parameters to experimental data. We also calculate various effective isotropic elastic properties from our single crystal MD results and study their temperature dependence as a substitute for first principles modeling of large polycrystalline systems. All the apatites have very comparable bulk, shear, and elastic moduli, but FAP has slightly higher values, and interestingly, HAP's Poisson's ratio shows no variation with temperature. This study sets the baseline with which any future studies on high-temperature applications of apatites (such as carbonate or radionuclide rich apatites) can be compared.

1. Introduction

Calcium phosphate apatites are the most commonly occurring natural phosphate minerals. As a primary source of phosphorus, they are utilized in a variety of applications, such as the production of fertilizers, animal food additives, detergents, and pesticides [1]. The chemical formula of calcium phosphate apatites is $[Ca_{10}[(PO_4)_6][X]_2]$, where the X sites are occupied by anions like Br^-, Cl^-, F^-, or OH^-. While apatites are typically found in hexagonal symmetry with $P6_3/m$ space group, the structure is highly flexible, allowing for several substitutions [2] in Ca and PO_4 sites. As may be guessed, due to such flexibility, multiple types of apatites are found naturally. Of them, the most prevalent ones are Fluorapatite (FAP), Hydroxyapatite (HAP), and Chlorapatite (ClAP), where the site X is occupied by F^-, OH^-, and Cl^-, respectively.

These three apatites have numerous biomedical applications: FAP and ClAP are often used in orthodontics [3], and HAP is widely used as a coating for orthopedic implants [4]. There is an increasing demand for these apatites in the environmental remediation industry to sequester CO_2 [5], heavy metals [6] and dyes [7], and to store radioactive wastes [8].

Some of these applications may involve high operating temperatures. For example, if one wants to sequester CO_2 directly from the source, one must consider the typical exhaust gas temperature of 400–600 K in automobiles and 700–800 K in thermal power plants [9]. For CO_2 sequestration, it has been shown that HAP absorbs CO_2, upon dehydroxylation, at a very high temperature range of 1100–1400 K [5]. Likewise, for immobilizing radionuclide waste in apatite matrix, a sintering temperature of 1300–500 K is needed [10].

While these diverse applications of calcium phosphate apatites are possible due to their unique macroscale mechanical properties, it is essential that an accurate estimate of these properties are available for an efficient and cost-effective adoption of these minerals. Due to their hexagonal structure, apatite crystals have five independent elastic constants. Nevertheless, as we review in the next section, experimental studies commonly report isotropic properties, and limited computational results available in the literature exhibit a large scatter. Moreover, investigation of temperature dependence of apatite elastic properties which would be essential for designing future applications is yet to be addressed in the current state of the art.

In this work, we evaluate the single crystal elastic constants of the three apatite structures: first from density functional theory (DFT) using ultrasoft pseudopotential with PBEsol exchange–correlation functional under generalized gradient approximation (GGA) on a single unit cell, and then with molecular dynamics (MD) using a core–shell based potential model at temperatures varying from 10 K to 1500 K. While DFT is considered to be more accurate than MD, but the first principle investigations are limited to ground states, although *ab initio* MD (AIMD) can be used to include temperature effects, but it is computationally very expensive. Also, the accuracy of DFT depends on several factors, including numerical tolerances (e.g., related to spatial discretization and k-point sampling), the choice of pseudopotential, and the exchange–correlation functional used. While numerical tolerances can be tightened to improve accuracy, the pseudopotential and exchange–correlation functional cannot be systematically improved. Higher rung functionals, such as hybrid functionals, offer greater accuracy but are computationally expensive, while semi-local functionals such as the generalized gradient approximation (GGA) offer a good balance between accuracy and computational efficiency. Nevertheless, even with a GGA functional, DFT is computationally expensive due to its inherent cubic-scaling cost relative to the system size (number of electrons). This prohibits the use of DFT for large-scale ground-state calculations, let alone for AIMD. On the other hand, MD simulations, being a linear-scaling method, can handle much larger systems. However, the accuracy of MD simulations is dependent on the interatomic potentials, and finding a suitable potential model for a desired system can be challenging. The choice of MD potential is based on our earlier study which revealed that the Buckingham-based potential for modeling the non-bonded interactions is best suited for understanding the elastic properties of apatites. With the absence of direct experimental data for hydroxyapatite (HAP) and chlorapatite (ClAP), and the scattered nature of available data for fluorapatite (FAP), DFT simulations serve as a reference point for validating our MD results at room temperature. In order to make the results consistent, we employ the same structure for both DFT and MD in our current work, along with the same family of inter-atomic potentials and convergence criteria for the three apatites.

This manuscript is organized as follows: Section 2 reviews and identifies gaps in the currently available experimental and computational data on apatite elastic properties. Section 3 details the MD and DFT simulations adopted for estimating the elastic constants and their related properties. Subsequently, our results are discussed in Section 4. We end this manuscript with our conclusions and way forward. We hope this work will set the baseline with which future studies on high-temperature applications of apatites (such as carbonate or radionuclide rich apatites) can be compared.

2. A brief review of reported elastic constants

Experimentally, determining the individual anisotropic elastic constants of apatites is challenging. Most of the studies have reported the effective isotropic elastic modulus of apatites, as may be seen in Table 1. An interesting observation can be made from Table 1: a wide scatter may be seen in the reported values of E. For FAP, E varies from 118.7 GPa to 146.6 GPa. The scatter is even more for HAP and ClAP. Such large scatter may be attributed to the differences in the density, geometry, crystallinity, grain size, and purity of the apatite samples along with the differences in the used experimental methods. For example, Gilmore and Katz [11] measured the ultrasonic velocities in compressed HAP powder under various pressures, extrapolated them to zero pressure to remove the influence of porosity, and based on their data the approximated (using VRH) $E =$ is 114 GPa. Currey [12], on the other hand, assumed the E value of HAP as 176 GPa to demonstrate that the elastic modulus of bones grows rapidly with mineral content, and reaches up to 15 GPa. Similarly for ClAP, the elastic modulus as determined by the nanoindentation technique [13], is reported to be 110 ± 15 GPa (using a weighted average across various directions), while according to the recent study by Zhang et al. [14], it is $\sim$ 42.7 GPa.

Table 1 also summarizes the experimental results on the five individual elastic constants of apatites: C_{11}, C_{12}, C_{13}, C_{33}, and C_{44}. It is likely that due to the difficulty in independently assessing them, only a few experimental results are available. As can be seen from the table, two divergent sets of elastic constants of FAP have been reported in the literature. Bhimasenachar [15] suggested that $C_{11} > C_{33}$, while Yoon et al. [16] and Sha et al. [17] independently assessed C_{33} to be greater than C_{11}. Further, it is important to note that no study, to the best of our knowledge, has reported the individual elastic constants of ClAP, and only one study has reported indirectly the elastic constants of HAP [18] where they are obtained by scaling the isotropic moduli of HAP against the corresponding moduli of FAP.

The need to accurately assess the different elastic constants, considering the inconsistencies with the experimental results, has necessitated their evaluation using computational methods. Of the different methods, electronic scale density functional theory (DFT) and atomic scale molecular dynamics (MD) simulations have been widely used by researchers. However, the accuracy of the results obtained using these methods depends on many factors, such as the underlying crystal structure (for both DFT and MD), the interatomic potential (for MD), the choice of exchange–correlation functional and pseudopotential (for DFT). For example, due to differences in the initial structure, the DFT results of Ching et al. [20] and Snyders et al. [21] for HAP, differ by $\sim$ 50% for C_{12} and by 33% for C_{33}, as is evident from Table 2. Similar differences can also be observed in the MD results of HAP as well — Mostafa and Brown [22] and De Leeuw et al. [23] employed different potential parameters in MD simulations, which resulted in 25% and 18% differences in C_{33} and C_{11}, respectively. The differences are sufficient to change the relative ordering of the elastic constants C_{12}, C_{13}, and C_{44}. The inconsistency in the relative ordering is also observed among the MD and DFT results for FAP and ClAP. The variability and inconsistency of the reported data make it difficult to reliably estimate the other mechanical properties of these three apatites. Therefore, it is important to evaluate elastic constants consistently, taking into account their dependence on previously identified factors. It is also worth noting that the elastic constants of apatites stated above are only provided at the room temperature.

3. Computational methodology

This section outlines the procedure utilized in our investigation to determine the lattice parameters, the elastic constants and the associated elastic properties. Our goal in this study is to: (i) evaluate the five elastic constants of hexagonal HAP, FAP, and ClAP independently

Table 1
Reported experimental elastic constants (in GPa) along with reported/calculated values of B, G, v, and E. The calculated values are obtained through the Voigt–Reuss–Hill (VRH) averaging.

Type	C_{11}	C_{12}	C_{13}	C_{33}	C_{44}	B	G	v	E	Remarks
FAP	166.7	13.1	65.5	139.6	66.3	84.2	60.6	0.20	146.6	Ultrasonic technique [15]
	143.4	44.5	57.5	180.5	41	86.5	46.7	0.27	118.7	Ultrasonic pulse superposition method [16]
	152.0	49.7	63.1	185.8	42.8	92.7	47.9	0.27	122.8	Ultrasonic technique [17]
	–	–	–	–		94[a]	46.4[a]	0.29	120[a]	From elastic wave velocity through powders under pressure [11]
HAP	137.0	42.5	54.9	172.0	39.6	82.6	44.6	0.27	113.3	Approximation based on FAP's elastic constants [18]
	–	–	–	–	–	89[a]	44.5[a]		114	From measurement of elastic wave velocity through powders under pressure [11]
	–	–	–	–	–	–	–	–	62.8[a]	Microdeformation of bone filaments under torsional loading [19]
ClAP	–	–	–	–	–	–	–	–	42.7[a]	Nano-indentation technique [14]
	–	–	–	–	–	–	–	–	110 ± 15[a]	Nano-indentation technique [13]

[a] Correspond to the reported experimental values.

Table 2
Reported elastic constants (in GPa) of apatites from computational studies.

Type	C_{11}	C_{12}	C_{13}	C_{33}	C_{44}	B[a]	G[a]	v[a]	E[a]	Remarks
HAP	117.1	26.2	55.6	231.8	56.4	76.31	52.35	0.19	127.83	DFT study using Hexagonal unit cell [21].
	117.9	30.55	66.4	165.0	38.5	77.2	39.4	0.28	101.0	DFT study using Hexagonal unit cell [24].
	140.0	42.4	54.9	172.0	39.6	83.32	45.23	0.27	114.91	DFT study using orthorhombic unit cell [20].
	158.0	57.5	59.8	147	43.9	90.76	46.57	0.28	119.31	MD study based on core–shell model [22].
	134.4	48.9	68.5	184.7	51.4	89.63	46.48	0.27	118.89	MD study based on core–shell model [25].
FAP	126.3	36.2	63.4	167.6	34	80.7	39.2	0.29	101.3	DFT study on hexagonal unit cell [24].
	165.0	55.0	60.0	145.0	40.2	91.5	46.6	0.28	119.5	MD study based on core–shell model [22]
	150.6	62.8	73.6	176.6	53.2	99.2	47.6	0.29	123.2	MD study based on core–shell model [25].
ClAP	109.6	30.9	47.2	152.2	39.2	67.6	39.7	0.2	99.7	DFT study on hexagonal unit cel [26].
	126.7	77.6	38.6	176.0	49.1	82.0	51.9	0.23	128.63	MD study based on core–shell model [27].

[a] are obtained from VRH approximation.

using both DFT and MD, (ii) utilize the evaluated elastic constants to calculate related mechanical properties — isotropic elastic modulus, bulk modulus, and shear modulus, and (iii) identify the temperature dependence of the elastic constants and the related mechanical properties. Considering that very few experimental studies have focused on studying the single crystal elastic constants of apatites, we use the DFT results as the benchmark for comparison with our MD results. In order to avoid the discrepancies associated with the different initial structures, in the present work, we use the same structure for both DFT as well as MD, along with the same family of inter-atomic potentials and convergence criteria for the three apatites.

3.1. Structural details

The baseline structures of the three apatites, which form the basis for all of our simulations, are described first. The geometry of the apatites used in this work belongs to the P6$_3$/m space group and has a hexagonal structure. This system comprises two equal crystallographic axes, $a = b$ (the basal plane lattice parameters i.e, the edge lengths of the basal plane of the hexagon) and the third axis, c, (height of the unit cell) which is perpendicular to the basal plane. In literature, HAP and ClAP are also found in the monoclinic space group P2$_1$/b, depending on the stoichiometry, temperature, and synthesis pressure [28,29]. The variations between the models are due to the differences in the local ordering of the anion groups (OH$^-$,F$^-$, Cl$^-$) and minor deformation of the phosphate tetrahedra. For our study, we used the experimental data given by Hughes et al. [30] in the P6$_3$/m space group as an initial guess of the pristine apatite structures. This structure has been utilized in numerous theoretical investigations. Mostafa and Brown [22], for example, employed it to generate the potential model for the FAP and HAP, Snyder et al. [21] also used it to investigate nanoscale deformation processes in bulk hexagonal HAP under uniaxial pressure.

It should be noted that the HAP and ClAP structures have a disorder at the OH$^-$ and Cl$^-$ locations due to the two mirror planes at $\frac{1}{4}c$ and $\frac{3}{4}c$. As a result of this disorder, the number of OH$^-$ and Cl$^-$ ions per unit cell doubles with partial occupancy. This problem is circumvented by removing the excess hydroxyl and chloride groups. FAP does not show such partial occupancy as the F$^-$ ions are situated on the mirror planes. A schematic representation of the unit cells for the three different apatites is depicted in Fig. 1, along with the crystallographic axes. The initial coordinates of each structure are given in the Supplementary Material. While the base structure for the three apatites are the same, the fractional coordinates of chloride ions along the c axis are different from those of hydroxyl and fluoride ions. The potential energy of ClAP is found to be minimum (not shown) when the fractional coordinates of the two chloride ions are 0.00 and 0.50 along the c axis instead of 0.25 and 0.75. Thus, we take the configuration of ClAP shown in Fig. 1(c) for the remainder of this study. All of our MD simulations make use of a 5 × 5 × 5 supercell, while our DFT study uses a single unit cell of pristine apatite structures.

3.2. Computation of elastic properties

In the elastic limit, the generalized Hooke's law relates stresses with strains through the relation:

$$\sigma_{ij} = C_{ijkl}\epsilon_{kl}, \tag{1}$$

where, σ_{ij} and ϵ_{ij} are the components of the stress and the strain tensor, respectively, and C_{ijkl} represents the components of the constitutive matrix. Due to the symmetry of hexagonal crystals, the constitutive matrix of apatites can be expressed in terms of five independent constants,

$$C = \begin{pmatrix} C_{1111} & C_{1122} & C_{1133} & 0 & 0 & 0 \\ C_{1122} & C_{1111} & C_{1133} & 0 & 0 & 0 \\ C_{1133} & C_{1133} & C_{3333} & 0 & 0 & 0 \\ 0 & 0 & 0 & C_{2323} & 0 & 0 \\ 0 & 0 & 0 & 0 & C_{2323} & 0 \\ 0 & 0 & 0 & 0 & 0 & C_{1212} \end{pmatrix}$$
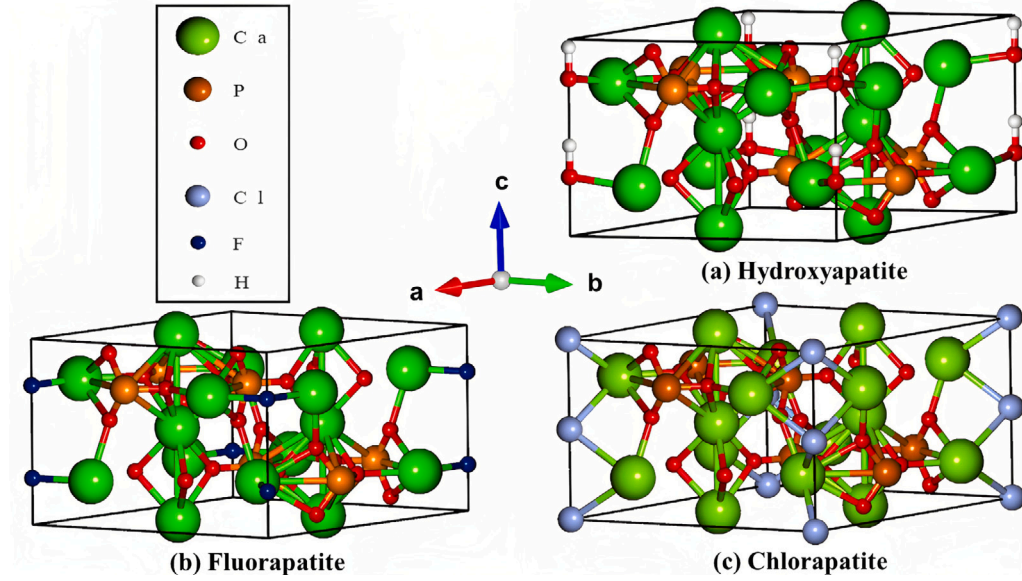
Fig. 1. A schematic representation of apatite unit cells: (a) Hydroxyapatite, (b) Fluorapatite, and (c) Chlorapatite, where a, b, c are the lattice parameters as mentioned in Section 2.1.

Table 3
Imposed strains and their corresponding relationship with stresses and strain energy density. Adopted from [24].

Imposed strain(s)	Non-zero stress(es)	Strain energy density
ϵ_1	$\sigma_1 = C_{11}\epsilon_1$ $\sigma_2 = C_{12}\epsilon_1$ $\sigma_3 = C_{13}\epsilon_1$	$U = \frac{1}{2}C_{11}\epsilon_1^2$
$\epsilon_1 = \epsilon_2$	$\sigma_1 = \sigma_2 = (C_{11} + C_{12})\epsilon_2$ $\sigma_3 = 2C_{13}\epsilon_2$	$U = (C_{11} + C_{12})\epsilon_1^2$
ϵ_3	$\sigma_1 = \sigma_2 = C_{13}\epsilon_3$ $\sigma_3 = C_{33}\epsilon_3$	$U = \frac{1}{2}C_{33}\epsilon_3^2$
$\epsilon_1 = \epsilon_3$	$\sigma_1 = (C_{11} + C_{13})\epsilon_1$ $\sigma_2 = (C_{12} + C_{13})\epsilon_1$ $\sigma_3 = (C_{13} + C_{33})\epsilon_1$	$U = \frac{1}{2}(C_{11} + 2C_{13} + C_{33})\epsilon_1^2$
ϵ_4	$\sigma_4 = 2C_{44}\epsilon_4$	$U = C_{44}\epsilon_4^2$

$$= \begin{pmatrix} C_{11} & C_{12} & C_{13} & 0 & 0 & 0 \\ C_{12} & C_{11} & C_{13} & 0 & 0 & 0 \\ C_{13} & C_{13} & C_{33} & 0 & 0 & 0 \\ 0 & 0 & 0 & C_{44} & 0 & 0 \\ 0 & 0 & 0 & 0 & C_{44} & 0 \\ 0 & 0 & 0 & 0 & 0 & C_{66} \end{pmatrix} \quad (2)$$

The matrix following the last equality shows the elastic constants in Voigt notation. In Voigt notation, the index 11 is replaced by 1, 22 by 2, 33 by 3, 23 (and 32) by 4, 13 (and 31) by 5, and 12 (and 21) by 6. These five independent elastic constants can be estimated by subjecting the system to five independent strains. Table 2 shows the applied strains, and their relationships with stresses and strain energy density [24]. One can estimate the elastic constants through either of the two relations, with negligible differences [24]. Except for the imposed strains, all other strains are kept zero. Straining the system in this manner ensures that extremely low symmetry structures do not emerge, which is a possibility if random strains are applied to the system. In such low symmetry structures, it is difficult to compute the energy, particularly with DFT, necessitating more computing time.

3.2.1. Effective isotropic elastic properties

Polycrystalline materials comprise randomly oriented and shaped single crystal grains. For all practical purposes, the polycrystals can be considered homogeneous and isotropic at the macroscopic scale. However, calculating the elastic properties of such polycrystalline systems using atomistic-scale simulations is challenging. One needs to consider a large number of samples to average out the behavior due to the random orientation and shape of the individual grains. This makes the entire task computationally expensive. The problem can be circumvented if one can calculate the isotropic properties from single-crystal elastic constants. For this purpose, researchers have typically used the VRH approximation, which we detail next.

The elastic (C) and the compliance (S) tensor components for an isotropic material can be written as:

$$C_{iijj} = B\delta_{ii}\delta_{jj} + G(\delta_{ii}\delta_{ij} + \delta_{ij}\delta_{ij} - \frac{2}{3}\delta_{ii}\delta_{jj}),$$
$$S_{ijkl} = \frac{1}{9B}\delta_{ij}\delta_{kl} + \frac{1}{4G}(\delta_{ik}\delta_{jl} + \delta_{il}\delta_{jk} - \frac{2}{3}\delta_{ij}\delta_{kl}) \quad (3)$$

Here, B and G represent the bulk and the shear modulus, respectively. Being fourth-order tensors, both C and S have two linear invariants, which remain unchanged under coordinate transformation:

$$\sum_{i,j} C_{iijj} = 9B, \quad \sum_{i,j} C_{ijij} = 3B + 10G, \quad \sum_{i,j} S_{iijj} = \frac{1}{B},$$
$$\sum_{i,j} S_{ijij} = \frac{1}{3B} + \frac{5}{2G}. \quad (4)$$

Henceforth, Voigt notation is used in this manuscript to write these tensors in a compact form.

Considering a polycrystalline material as homogeneous on a macroscopic level, we can approximate its overall average properties by an effective medium. After taking volume average of Eq. (1), we can write,

$$\langle\sigma_i\rangle = \langle C_{ij}\epsilon_j\rangle \quad , \quad \langle\epsilon_i\rangle = \langle S_{ij}\sigma_j\rangle \quad (5)$$

Let this polycrystal be subjected to a macroscopic stress of Ξ which results in a macroscopic strain of ϵ. Let σ and ϵ be the microscopic stress and strain at any point of any grain. From the principle of virtual work, we can write:

$$\Xi \cdot \epsilon = \frac{\int \sigma \cdot \epsilon dV}{\int dV} \quad (6)$$

When the microscopic strain is ϵ, let the corresponding microscopic stress be σ^*. Likewise, for the microscopic stress Ξ, the microscopic

strain in grains is ϵ^*. Using Maxwell's reciprocal theorem, Hill [31] argued that the following equations:

$$\sigma \cdot \epsilon + (\sigma - \sigma^*) \cdot (\epsilon - \varepsilon) \equiv \sigma^* \cdot \varepsilon + 2(\epsilon - \varepsilon) \cdot \sigma,$$
$$\sigma \cdot \epsilon + (\sigma - \Xi) \cdot (\epsilon - \epsilon^*) \equiv \Xi \cdot \epsilon^* + 2(\sigma - \Xi) \cdot \epsilon \tag{7}$$

can be written as:

$$\sigma \cdot \epsilon \leq \sigma^* \cdot \varepsilon + 2(\epsilon - \varepsilon) \cdot \sigma \quad , \quad \sigma \cdot \epsilon \leq \Xi \cdot \epsilon^* + 2(\sigma - \Xi) \cdot \epsilon \tag{8}$$

due to the positive nature of strain energy. In Voigt approximation [32], the microscopic strain, ϵ, is assumed to the same as the macroscopic strain, ε. On the other hand, in Reuss approximation [33], the microscopic stress, σ, is assumed to the same as the macroscopic stress, Ξ. Therefore, Eq. (8), under the Voigt and Reuss approximations, can be simplified to:

$$\Xi \cdot \epsilon \leq \frac{\varepsilon \cdot \int \sigma^* dV}{\int dV} \quad , \quad \Xi \cdot \epsilon \leq \frac{\Xi \cdot \int \epsilon^* dV}{\int dV}. \tag{9}$$

The left-hand side of this equation represents twice the real energy density and the right-hand side represents twice the energy densities computed by the Voigt and Reuss theories, respectively. Rewriting Eq. (9) using Eqs. (1) and (3), we get:

$$B \sum_{i=1}^{3} \epsilon_i^2 + \frac{2}{3} G \sum_{i \neq j} (\epsilon_i - \epsilon_j)^2 \quad \leq \quad B_V \sum_{i=1}^{3} \epsilon_i^2 + \frac{2}{3} G_V \sum_{i \neq j} (\epsilon_i - \epsilon_j)^2$$
$$\frac{1}{B} \sum_{i=1}^{3} \Xi_i^2 + \frac{3}{2G} \sum_{i \neq j} (\Xi_i - \Xi_j)^2 \quad \leq \quad \frac{1}{B_R} \sum_{i=1}^{3} \Xi_i^2 + \frac{3}{2G_R} \sum_{i \neq j} (\Xi_i - \Xi_j)^2 \tag{10}$$

The suffix R and V denote the approximated moduli based on Reuss and Voigt approximation, respectively. Eq. (10) is true for any stress–strain, so we can write,

$$B_R \leq B \leq B_V \quad , \quad G_R \leq G \leq G_V \tag{11}$$

The mathematical expression of bulk (B_V) and shear modulus (G_V) for a hexagonal crystal under Voigt approximation can be obtained using Eq. (4):

$$B_V = \frac{1}{9} \left[(2C_{11} + C_{33}) + 2(C_{12} + 2C_{13}) \right],$$
$$G_V = \frac{1}{15} \left[(2C_{11} + C_{33}) - (C_{12} + 2C_{13}) + 3(2C_{44} + C_{66}) \right]. \tag{12}$$

Similarly, the Reuss bound of bulk (B_R) and shear modulus (G_R) can be obtained as:

$$B_R = \frac{(C_{11} + C_{12})C_{33} - 2C_{13}^2}{C_{11} + C_{12} - 4C_{13} + 2C_{33}},$$
$$G_R = \frac{5[(C_{11} + C_{12})C_{33} - 2C_{13}^2]C_{44}C_{66}}{6B_V C_{44}C_{66} + 2[(C_{11} + C_{12})C_{33} - 2C_{13}^2]}. \tag{13}$$

Hill proposed to take the average of Voigt and Reuss bounds to evaluate the isotropic elastic constants of polycrystals-

$$B = \frac{1}{2}(B_R + B_V) \text{ and } G = \frac{1}{2}(G_R + G_V) \tag{14}$$

The elastic modulus E and Poisson's ratio ν for an isotropic material can be computed from the Hill's values of B and G using the following expressions,

$$E = \frac{9BG}{3B + G} \text{ and } \nu = \frac{3B - 2G}{6B + 2G} \tag{15}$$

3.3. Ab-initio simulation

Ab-initio calculations are performed using Quantum Espresso [34], a plane wave pseudopotential [35] DFT implementation. The accuracy of DFT calculations is significantly influenced by the selection of the exchange–correlation functional. Under generalized gradient approximation (GGA), certain functionals with increased gradient dependency can improve atomization and total energies but degrade

Table 4
Core–shell parameters for apatites. Adopted from de Leeuw et al. [23].

Atom type	Core charge	Shell charge	Lk_{CS} (eV Å^{-2})
Ca	2.000	–	–
P	1.180	–	–
O(P)	0.587	−1.632	507.40
O(H)	0.900	−2.300	74.92
H	0.400	–	–
F	0.400	–	–
Cl	0.400	–	–

bond lengths [36,37], while functionals with reduced gradient dependency can improve lattice parameters and surface energies but degrade total and atomization energies [38]. No GGA functional can excel at both [39], so a practical approach is necessary for lattice properties. Perdew et al. suggested a modified functional for solids [39] that restores the gradient expansion for exchange, resulting in better lattice constants compared to PBE [40] and excellent jellium surface exchange energies. Numerical investigations indicate that PBEsol can accurately compute bulk exchange energies of metals within the pseudopotential approximation. So, in our study we employed PBEsol exchange–correlation functional and the interaction between the ion cores and valence electrons in our study is accounted for through the ultra-soft pseudopotential [41].

The lattice parameters are computed by relaxing the unit cell using the variable-cell relaxation technique. We use 0.3 kbar as the convergence threshold for pressure, 10^{-6} Ry for energy, and 10^{-5} Ry/bohr for force for all DFT simulations. Once the convergence requirements are met, the lattice parameters are then retrieved directly. The relaxed structures are then individually subjected to five independent different strains to get the elastic constants, as described through Table 2. For each type of strain, seven separate values of strain are considered: $\epsilon_i = 0, \pm 0.25\%, \pm 0.50\%,$ and $\pm 0.75\%$ using a displacement controlled approach. In this approach, the lattice parameters in the desired directions are changed (increased or decreased). The strained system is subjected to energy minimization using the BFGS method of Quantum Espresso (QE). The elastic constants are then obtained from the stress–strain relations shown in Table 3.

3.4. Finite temperature molecular dynamics simulation

All MD simulations are performed using the free-to-use software LAMMPS, and comprise a $4 \times 4 \times 6$ supercell with 4224 atoms for HAP and 4034 atoms for FAP/ClAP. Several potential models for apatites have been proposed in the literature [25,42,43]. Based on our earlier work [44], the apatites are modeled through the core–shell-based Buckingham potential. In this potential, any ion is described as a combination of a heavy core and a massless shell. The core, with charge Q, symbolizes the atom's nucleus, while the shell, with charge q, approximates the valence electrons. The ion's total charge is the sum of Q and q. The core and its shell are connected by a harmonic spring so that the interaction energy is given by,

$$E(r_{CS,i}) = \frac{1}{2} k_{CS,i} r_{CS,i}^2. \tag{16}$$

Here, $k_{CS,i}$ is the force constant for the harmonic spring connecting the ith core–shell, and $r_{CS,i}$ is the distance between the core and the shell of the ith pair. The ion's exact location is determined by the position of the core. The position of the shell has no physical meaning even though its coordinates are initially the same as those of the core. The non-bonded interactions are described by the Buckhingham potential in conjunction with the Coulombic potential. The angle bending and

Table 5

Potential parameter by de Leeuw et al. [23] for apatites.

Non-bonded parameters				Bonded parameters				
Ion-pair	A (eV)	ρ (Å)	C (Å)	Atom-pair	D (eV) k (eVrad^{-2})	r_0 (Å) θ (deg)	α (Å)
Ca–O(H)	1250.00	0.343700	0.00	P–O(P)	3.470000	1.6000	2.03
Ca–O(P)	1550.00	0.297000	0.00	H–O(H)	7.052500	0.9485	3.1749
O(P)–O(P)	16372.00	0.213000	3.47	O(P)–P–O(P)	1.300626	109.4700	
O(P)–O(H)	22764.00	0.149000	4.92				
O(H)–O(H)	22764.00	0.149000	6.97				
H–O(P)	312.00	0.250000	0.00				
H–O(H)	312.00	0.250000	0.00				
F–F	99731834.00	0.120130	17.02				
Ca–F	1272.80	0.299700	0.00				
O(H)–F	35000.00	0.175000	15.40				
O(P)–F	583833.70	0.211630	7.68				
Cl–Cl	49039.26	0.243207	16.05				
Ca–Cl	1285.14	0.348729	0.00				
O(H)–Cl	71379.71	0.227705	0.13				
O(P)–Cl	68297092.09	0.153267	15.16				

bond stretching are modeled through harmonic and Morse potential, respectively. Mathematically, the potential can be expressed as:

$$\phi_{\text{BUCK}} = \sum_{\text{bonds}} D_{ij}(1 - \exp(-\alpha(r_{ij} - r_0)))^2 - D_{ij} + \sum_{\text{angles}} \frac{k_\theta}{2}(\theta_{ijk} - \theta_0)^2 +$$
$$+ \sum_{ij}\left(\left[A_{ij}\exp\left(-\frac{r_{ij}}{\rho_{ij}}\right) - \frac{C_{ij}}{(r_{ij})^6}\right] + \frac{1}{4\pi\epsilon_0}\frac{q_i q_j}{r_{ij}}\right)$$
$$+ \sum_i \frac{k_{CS,i}}{2}r_{CS,i}^2$$

(17)

where, $D_{i,j}$ is the bond enthalpy, r_0 is the equilibrium bond length, k_θ is the force constant and $(\theta_{ijk} - \theta_0)$ is the deviation from the equilibrium angle θ_0. In this study, we use the force field parameters proposed by de Leeuw et al. (cite), which may be seen in Tables 4 and 5. Due to implementation issues, we consider the P–O interactions of phosphate group as non-bonded Morse type with parameters remaining the same as shown in table, but with a cutoff equaling 2.0 Å.

The time step used for all MD simulations is 0.2 fs. Using the Nosé–Hoover thermostat [45], the system is initially equilibrated for 50 ps at the target temperature (NVT). Following the NVT runs, the system is subjected to a constant temperature and pressure (NPT) environment for 30 ps. The system is kept at the desired temperature for these NPT runs, and the pressure is set to 1 atm. It should be noted that the "aniso" option of LAMMPS has been selected for pressure control, which controls the pressure in the x, y, and z directions independently. The simulations are performed for the temperature range 10–1500 K.

The optimized lattice parameters (a, b, and c) are determined from the relaxed structure obtained during the NPT runs. The parameters a and c are directly calculated by dividing the time-averaged simulation box length (obtained across all the NPT runs) along the x and z directions by the corresponding number of unit cells along those directions, respectively (4 and 6, respectively,). The time-averaged simulation box length along the y direction is divided by the product of the number of unit cells along the y direction and the tilt ($4\cos 30°$ in our example) to obtain the lattice parameter b.

The relaxed structure is used to calculate the elastic constants. The relaxed structure is initially subjected to 50 ps of NVT runs at the target temperature. The system is then continuously strained (up to ±1.5%) in accordance with the loading directions specified in Table 3. The strain rate is set at 10^6/s in all cases. The xy direction is subjected to zero pressure and the desired temperature regardless of the loading. This type of pressure control is not employed in other directions. It should be noted that under these simulation settings, we receive zero stress in all directions except those listed in table. For example, when ϵ_1 is used, the non-zero stress components are σ_1, σ_2, and σ_3, as would be expected for a hexagonal crystal.

Table 6

Predicted lattice parameters from DFT and MD study.

Lattice parameters of structure of interest (in Å)				
Type		a	b	c
HAP	Experimental [30]	9.417	9.417	6.875
	DFT	9.390	9.398	6.819
	MD	9.389	9.389	6.857
FAP	Experimental [30]	9.397	9.398	6.878
	DFT	9.339	9.339	6.831
	MD	9.367	9.372	6.903
ClAP	Experimental [30]	9.593	9.593	6.776
	DFT	9.693	9.693	6.622
	MD	9.327	9.368	6.939

4. Results

First, we discuss and compare the equilibrium lattice parameters obtained from DFT and MD simulations with the available experimental data. The temperature dependence of the lattice parameters is also addressed. Following that, a similar analysis is presented for the elastic constants. Lastly, the temperature variation of the isotropic elastic properties – bulk modulus, shear modulus and elastic modulus – are discussed using the VRH approximation detailed earlier.

4.1. Lattice parameters

Table 6 presents the lattice parameters derived from the present study, as well as the results of other theoretical investigations and experimental measurements. In our study, the PBEsol exchange–correlation functional is employed, which is acknowledged for generating structural characteristics that are more comparable to experimental values when compared to PBE outcomes. For example, the lattice parameters of HAP are $a = b = 9.39$ Å and $c = 6.81$ Å, which deviate from the experimental data [30] by −0.2% for a and −0.8% for b. Likewise, The DFT-obtained lattice parameters of FAP differ from the experimental values ($a_e, b_e, c_e = 9.33, 9.33, 6.83$ in Å, respectively) marginally by −0.6%. Note that the subscript e is used to signify the experimental results. For ClAP, the lattice parameters obtained from DFT are: $a = b = 9.69$ Å and $c = 6.62$ Å. They differ from the experimental results by 1% and −2%, respectively.

Mirroring the DFT findings, the lattice parameters of the three apatites from room temperature MD simulations agree well with the experimental data; the absolute maximum error being smaller than 3%. For HAP, we find $a_0 = b_0 = 9.38$ Å, and $c_0 = 6.89$ Å, the subscript 0 indicating room temperature. Defining the relative deviation of lattice parameters through the following equation:

$$\delta_a = \frac{a_0 - a_e}{a_e} \times 100, \delta_b = \frac{b_0 - b_e}{b_e} \times 100, \text{ and } \delta_c = \frac{c_0 - c_e}{c_e} \times 100, \quad (18)$$
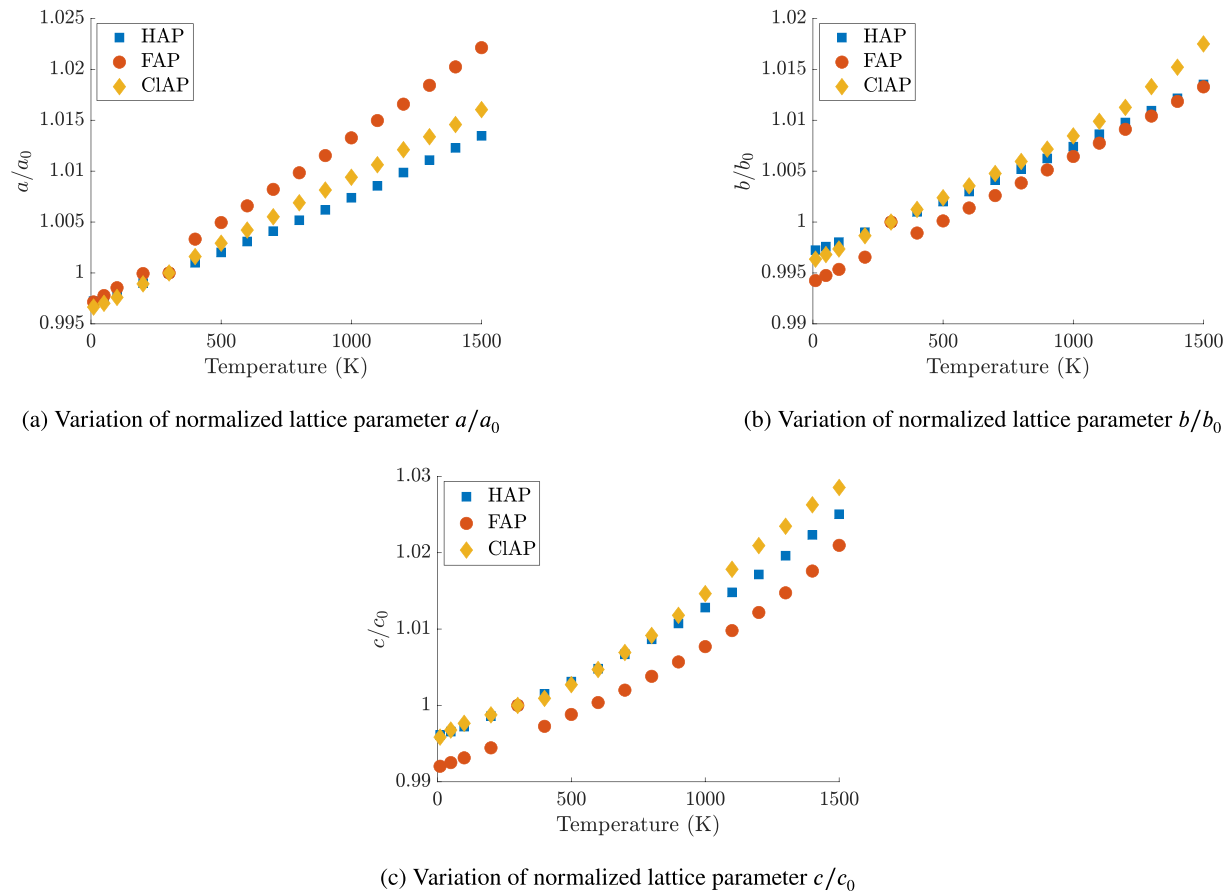
(a) Variation of normalized lattice parameter a/a_0

(b) Variation of normalized lattice parameter b/b_0

(c) Variation of normalized lattice parameter c/c_0

Fig. 2. Normalized lattice parameters as a function of temperature: (a) a/a_0, (b) b/b_0, and (c) c/c_0. The parameters a_0, b_0 and c_0 indicate the lattice constants at room temperature.

the deviations with respect to the experimental results are: $\delta_a = -0.28$ %, $\delta_b = -0.29$ % and $\delta_c = 0.26$ %. Similarly, for FAP and ClAP, the deviation from the experimental data are: $\delta_a = -0.31\%$, $\delta_b = -0.27\%$, and $\delta_c = 1.71\%$, and $\delta_a = -2.77\%$, $\delta_b = -2.90\%$, and $\delta_c = 2.41\%$, respectively. The temperature dependence of the normalized lattice parameters (a/a_0, b/b_0, and c/c_0), obtained from our MD simulations, is shown in Fig. 2. The normalized cell parameters increase as the temperature increases which is an expected behavior in any anharmonic system. Interestingly, the rate of increase of the different lattice parameters with temperature depends on the type of apatite: while in FAP a/a_0 grows faster, change in b/b_0 and c/c_0 is less than other apatites. We may infer from comparing the radial distribution functions of various elements that the P–P distance varies significantly as the temperature increases, but that the P–O and Ca–O bonds do not significantly vary with temperature.

4.2. Single crystal elastic constants

Apatites have five independent elastic constants: C_{11}, C_{12}, C_{13}, C_{33}, and C_{44}. While the elastic constants C_{11} and C_{33} reflect the unidirectional resistance towards deformation along the principal crystallographic axes a and c, respectively, the elastic constants C_{12} and C_{13} couple a normal stress component along the crystallographic a axis with a uniaxial strain along the crystallographic b and c axes. The last independent elastic constant, C_{44}, couples the shear stresses with the shear strains.

The single crystal elastic constants obtained from the DFT simulations are shown in Table 7. All three apatites have a higher C_{33} value than any other elastic constants, which implies the c-axis to be the stiffest. Even though the elastic constants of these apatites are similar, which is expected given that they all have the same structure, FAP is

Table 7
Predicted elastic constants from DFT and MD study (at room temperature) (in GPa)

Type		C_{11}	C_{12}	C_{13}	C_{33}	C_{44}
Single crystal elastic constants of structures of interest obtained in this work						
HAP	Experimental [18]	137.00	42.50	54.90	172.00	39.60
	DFT	136.50	39.90	70.50	182.70	35.80
	MD	130.30	47.10	65.70	174.70	48.70
FAP	Experimental [16]	143.40	44.50	57.50	180.50	41.00
	DFT	146.90	46.50	67.50	186.80	39.30
	MD	146.65	63.55	63.48	162.80	48.65
ClAP	Experimental	-	-	-	-	–
	DFT	115.70	29.40	64.30	180.70	42.60
	MD	139.70	55.84	54.49	160.70	45.97

found to have the highest value of all elastic constants, except C_{13} and C_{44}, among the three apatites. The relative ordering of the different elastic constants for FAP: $C_{13} > C_{12} > C_{44}$ corresponds well with the previous theoretical data based on DFT [24]. Interestingly, the relative ordering of these elastic constants change for ClAP: $C_{13} > C_{44} > C_{12}$ but for HAP the relative ordering is same as FAP: $C_{13} > C_{12} > C_{44}$. Further, the relative ordering of the elastic constants for HAP are in agreement with those reported by Katz and Ukraincik [18] $C_{13} > C_{12} > C_{44}$. It is worth noting that there is a significant amount of scatter in the experimental data as well, and the differences between our results and those of the experiments could be due to the structural differences, such as the presence of impurities, defects, the temperature effect on defects, metastability, etc.

The elastic constants obtained from MD calculations agree well with the experimental data at room temperature. For example, our results and the experimental results of Katz and Ukraincik [18] for
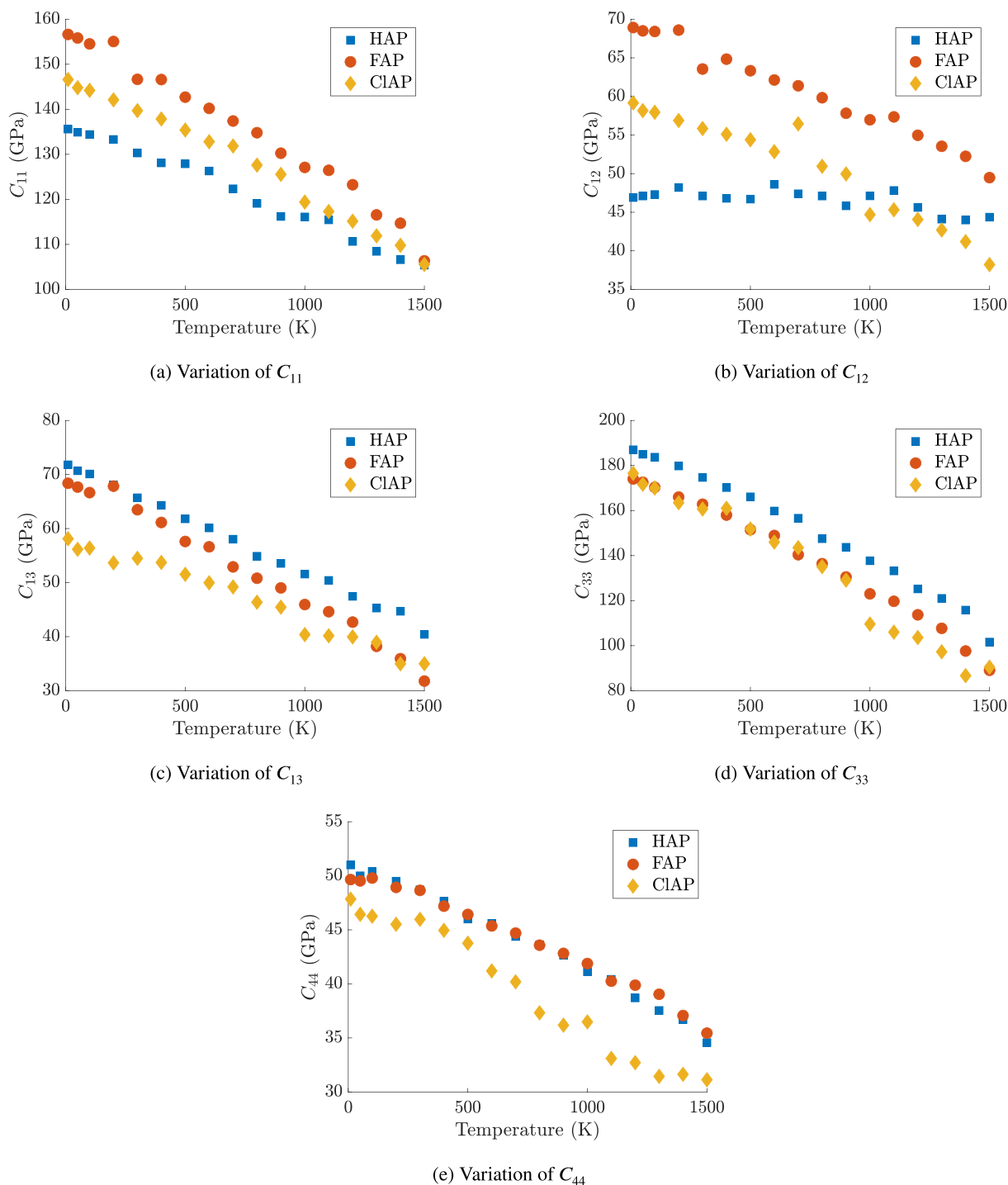
(a) Variation of C_{11}

(b) Variation of C_{12}

(c) Variation of C_{13}

(d) Variation of C_{33}

(e) Variation of C_{44}

Fig. 3. Temperature variation of the five single crystal elastic constants.

HAP show a good match. Likewise, for FAP, a good agreement can be seen with the experimental results of Yoon and Newnhman [16] and Sha et al. [17], with the exception of C_{12} and C_{44}, for which the deviations are $\sim$ 43% and 18%, respectively. Due to the lack of experimental data for ClAP, we cannot compare our MD results with experiments. The elastic constants obtained from MD and DFT show good agreement, except for C_{12} in all three apatites, where the difference exceeds 20%. It is worth noting that the relative ordering of C_{12}, C_{13}, and C_{44} is not consistent between the results obtained from DFT and MD. These discrepancies may be understood by looking into the calibration of MD potential parameters. Primarily, a variety of experimental data itself has been used to obtain these parameters. For

example, the Ca–O interaction parameters [46] have been determined by empirically fitting the experimentally obtained structural properties, elastic constants, and vibrational frequencies. Likewise, the Ca–F, P–O and O–O interactions have also been obtained from the experimental data [27].

Figs. 3 depicts the temperature dependence of the elastic constants of apatites over the temperature range of 10 K–1500 K. Five important observations can be made from these figures: (i) all elastic constants decrease with an increase in temperature, (ii) C_{11} is always less than C_{33} at low temperature, showing that it is easier to compress along the $\langle 100 \rangle$ direction than along the $\langle 001 \rangle$ direction, (iii) at high temperatures (> 900 K), $C_{33} < C_{11}$ for FAP and ClAP, which suggests that the more

Table 8

Predicted elastic properties from DFT: the bulk modulus, *B*, the shear modulus, *G*, the elastic modulus, *E*, and the Poisson's ratio, *ν*.

Type	B (GPa)	G (GPa)	E (GPa)	ν
HAP	88.31	41.68	108.05	0.29
FAP	92.34	45.26	116.71	0.28
CLAP	76.45	42.07	106.66	0.26

compressible direction changes at higher temperature, (iv) C_{12} of HAP does not vary significantly with temperature, which is not the case for the other two apatites, and the values deviate significantly from that at the room temperature, and (v) the rate at which the elastic constants change depend on the type of apatite, especially for C_{12} and C_{44}. Regardless of the temperature, the elastic constants satisfy the mechanical stability requirements for hexagonal structures:

$$C_{44} > 0, \qquad C_{11} - C_{12} > 0, \qquad C_{33}(C_{11} - C_{12}) - 2C_{13}^2 > 0. \qquad (19)$$

The relative ordering of C_{12}, C_{13} and C_{44} remains as $C_{12} > C_{13} > C_{44}$ for ClAP and FAP. This ordering, however, changes to $C_{12} > C_{44} > C_{13}$ at extremely high temperatures for FAP. While for HAP, the relative ordering is $C_{13} > C_{44} > C_{12}$ for temperature below 500 K, it changes to $C_{13} > C_{12} > C_{44}$ at high temperatures.

The highly anisotropic nature of apatites dictates the calculation of degree of elastic anisotropy. A mismatch of elastic constants in the surrounding crystals of a polycrystalline or a multiphase ceramic can increase the propensity of microcrack formation during loading, and can lead to early failure. One can estimate the degree of anisotropy from the calculated elastic constants by evaluating the shear anisotropic factors (SAFs). The SAF for the {100} plane between ⟨011⟩ and ⟨010⟩ directions is:

$$A_{100} = \frac{4C_{44}}{C_{11} + C_{33} - C_{13}}, \qquad (20)$$

and, for the 001 plane, between ⟨110⟩ and ⟨120⟩ directions is:

$$A_{001} = \frac{4C_{66}}{C_{11} + C_{22} - C_{12}} \qquad (21)$$

In an isotropic material, A_{100} and A_{001} must all be equal to unity. For all apatites, we find the SAFs to deviate from unity in the prismatic plane (A_{100}). But, in the basal plane (A_{001}), SAF is equal to one for all three apatites, which agrees with the general property of hexagonal materials.

The knowledge of single crystal elastic constants can also be used to calculate the Cauchy pressure, $C_{12} - C_{44}$, which is closely related to the ductile characteristics of a material. A ductile (brittle) material has $C_{12} - C_{44} > 0 (< 0)$ [47]. Apatites, on account of being minerals, are expected to be brittle. However, only HAP is found to be brittle from MD simulations at temperatures < 500 K and ductile from DFT simulations. Surprisingly, at all temperatures, both FAP and ClAP have $C_{12} - C_{44} > 0$.

4.3. Isotropic material properties

We now look at the temperature dependence of the following isotropic elastic properties — bulk modulus, shear modulus, elastic modulus, and Poisson's ratio.

4.3.1. Bulk and shear moduli

The bulk modulus, *B*, and the shear modulus, *G*, obtained from DFT simulations are listed in Table 8. As may be seen from the table, both bulk and shear moduli of the apatites are similar: the difference between the largest and the smallest values is ∼ 15 GPa for *B* and ∼ 4 GPa for *G*. Of the three apatites, ClAP is the most compressible one (*B* = 76.45 GPa), while HAP has the smallest value of *G* = 41.68 GPa. Interestingly, FAP is the least compressible apatite (*B* = 92.34 GPa) and

also the most resistant to shear deformation (*G* = 45.26 GPa). DFT results are in good agreement with the experimental investigations [18]. The relative compressibilities of the different apatites are in agreement with the experimental results. For instance, the DFT results maintain the findings of Gilmore and Katz [11] that the bulk modulus of FAP is higher than that of HAP. Such an agreement is not evident for *G*.

At room temperature, the bulk modulus of HAP, FAP, and ClAP from MD simulations are 86.36 GPa, 92.91 GPa, and 85.38 GPa, respectively. The corresponding shear moduli are: 44.62 GPa, 45.34 GPa, and 45.01 GPa. These results are in good agreement with the experimental results of Gilmore and Katz [11]. Likewise, the results are in good agreement with the MD results of de Leeuw et al. [22,23,27]. Similar to our DFT studies, the MD results also indicate a consistent relative ordering of the bulk moduli of the three apatites: $B_{FAP} > B_{HAP} > B_{ClAP}$. The temperature dependence of *B* and *G* for all three apatites are shown in Figs. 4(a) and 4(b), respectively. In the temperature range of 10–1200 K, FAP has a higher resistance to volumetric changes than either HAP or ClAP. However, at even higher temperatures (1300–1500 K), HAP has a greater *B* value than FAP. We observe ClAP to be the most susceptible amongst the three apatites to volumetric changes, regardless of the temperature. In comparison to 10 K, *B* falls by about 45%–50% at 1500 K. Unlike *B*, throughout the temperature range investigated, FAP has the highest shear modulus. While at lower temperatures, the shear moduli of ClAP and HAP are almost identical, at higher temperatures, shear modulus of ClAP decreases faster than HAP. In comparison to 10 K, the shear modulus decreases by ∼33% at 1500 K.

The knowledge of *B* and *G* can be used to quickly identify other mechanical properties. For example, the criterion proposed by Pugh [48] uses *B/G* ratio to understand the ductility characteristics, and an estimate of Vicker's hardness can be obtained from the value of *G*. Adopting Pugh's criterion for apatites suggests that *B/G* > 1.75 at all temperatures. With increasing temperature, Vicker's hardness is found to decrease for the different apatites.

4.3.2. Elastic modulus and Poisson's ratio

The elastic moduli of the three apatites, predicted by the DFT analyses, are in range between 106 GPa and 116 GPa. At room temperature, the MD simulations predict *E* = 114.21 GPa, 117.00 GPa, and 114.86 GPa for HAP, FAP and ClAP, respectively. The results of HAP and FAP are in good agreement with the reported value of *E* [11]. These findings indicate that FAP has the highest elastic modulus among the three apatites, and the trend is corroborated by both the experimental data and our DFT investigations. Temperature variation of *E* is shown in Fig. 5(a). As we can see in this figure, with increasing temperature elastic modulus decreases for all three apatites. Irrespective of the temperature, FAP has the highest value of *E*. At temperatures below 500 K, the elastic modulus of ClAP and HAP are comparable, but at higher temperatures, they no longer remain comparable.

Now, let us look at Poisson's ratio, which is the ratio of transverse strain to axial strain when a material is subjected to uniaxial tension. The results obtained from our DFT calculations may be seen in Table 8. The values are comparable for the three apatites, and a similar trend is observed from our MD simulations at room temperature. The temperature variation of Poisson's ratio is depicted in Fig. 5(b). Most ceramics show a clear variation of Poisson's ratio with temperature, for example, fused quartz, ZrB_2, HfB_2, TiB_2 [49] etc Poissons ratio increases with increase in temperature. There is a marginal decrease in Poisson's ratio for FAP as the temperature increases.

5. Conclusions

We calculated the single crystal elastic constants of apatites through first-principles (DFT) and molecular dynamics (MD) based simulations, and subsequently studied their temperature dependence. The limited existing experimental and computational studies at room temperature
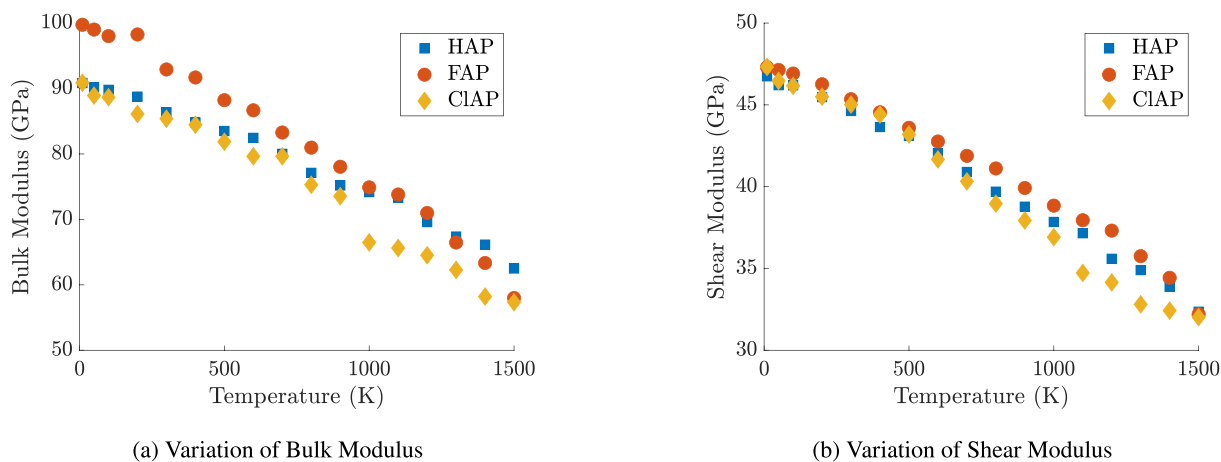
(a) Variation of Bulk Modulus

(b) Variation of Shear Modulus

Fig. 4. Temperature dependence of: (a) Bulk modulus and (b) Shear modulus.

(a) Variation of Elastic Modulus

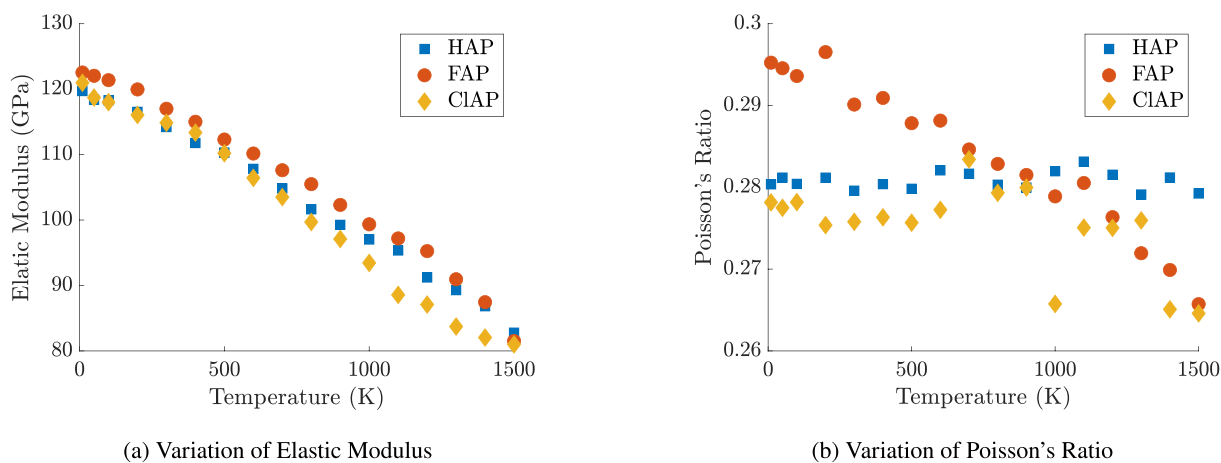(b) Variation of Poisson's Ratio

Fig. 5. Temperature dependence of: (a) Elastic modulus and (b) Poisson's ratio.

show a wide scatter due to the use of different methodology, initial structure, convergence criteria, etc. As a secondary objective, we evaluated the elastic constants and their temperature dependence in a consistent manner by using the same methodology, initial structure, and convergence criteria for all our DFT and MD simulations. Apart from the elastic constants, we also studied the temperature dependence of related mechanical properties — bulk modulus, shear modulus, elastic modulus, and Poisson's ratio. The main conclusions of our study are:

1. The obtained lattice parameters from both DFT and MD are in good agreement with the experimental and previously reported theoretical values. The normalized lattice parameters a/a_0, b/b_0, and c/c_0, increase with temperature. The P–P distance varies more noticeably with temperature, which may be the primary cause of the change in lattice parameters.

2. The published data based on DFT consistently underestimates the elastic constants of apatite. Researchers have tried with different implementations to see if the DFT results improve, but such approaches have not been very successful. For example, Menendez et al. [24], apart from considering the P6_3/m symmetry structure, also computed the elastic constants using the P2_1b symmetry structure with PBE [40] exchange–correlation functional, but could not find any discernible differences in the elastic constants due to the two structures. Likewise, the application of external pressure on the system also did not result in improved elastic constants for HAP. The primary reason for

such discrepancy is because of the usage of PBE exchange–correlation functional. PBE has a general tendency to underbind in solids [50–54], leading to overestimation of lattice constants and underestimation of elastic constants. As can be seen from our DFT results, making use of PBEsol exchange–correlation functional significantly improves the elastic constants, which are now in better agreement with the experimental results. This is because the PBEsol exchange–correlation functional is known to provide better estimates for bulk properties of solids. The DFT results indicate ⟨001⟩ to be the stiffest direction for all apatites, and FAP to be the stiffest among the three apatites.

3. Interestingly, the elastic constants obtained from the MD studies are in good agreement with the experimentally reported ones at room temperature. We attribute this to the fact that the parameters of the potential function are calibrated to the experimental results. Nevertheless, like DFT, MD also predicts $C_{33} > C_{11}$ for all three apatites, which changes to $C_{11} > C_{33}$ for FAP and ClAP at very high temperature. As the temperature rises, the elastic constants decrease but the rate is different for the different elastic constants. At 1500 K, C_{33} and C_{13} decrease by > 50% in comparison to their value at 10 K. Like the elastic constants, the isotropic properties such as elastic modulus, shear modulus and bulk modulus decrease with temperature. However, Poisson's ratio is relatively unaffected.

4. Our DFT investigation reveals that the relative ordering of the elastic constants for ClAP is $C_{13} > C_{44} > C_{12}$, but for HAP and FAP the following holds true: $C_{13} > C_{12} > C_{44}$. The trend

indicated by our DFT analysis is not reflected in our MD results; for ClAP and FAP, it is $C_{12} > C_{13} > C_{44}$. For HAP, the relative ordering for temperatures below 500 K is $C_{13} > C_{44} > C_{12}$, but at high temperatures, the trend becomes $C_{13} > C_{12} > C_{44}$. A clear idea about the relative ordering of these elastic constants is essential since the cleavage planes depend on it. Further, in bio-friendly functional materials such as liquid crystals made of HAP, the optical characteristics may change depending on the relative ordering.

5. Calculation of Cauchy pressure using MD simulations suggests that for HAP $C_{12} - C_{44} < 0$, which indicates brittleness, at temperatures below 500 K. The other two apatites show $C_{12} - C_{44} > 0$. Considering the fact that apatites are minerals, and hence, likely to be brittle, the usefulness of Cauchy pressure in case of minerals needs careful investigation. For this purpose, a full-scale MD simulation of uniaxial tensile test with polycrystalline apatite needs to be performed.

It needs to be noted that the potential parameters used in the MD calculation do not intrinsically include the temperature effect, the accuracy of the results cannot be judged as there are no experimental data available. However, this study provides useful insights for the further development of the applicability of apatites by providing an initial assessment of mechanical stability and elastic properties of apatites as a function of temperature.

CRediT authorship contribution statement

Aritri Roy: Generated and analyzed the results. **Bikash Kanungo:** Generated and analyzed the results. **Puneet Kumar Patra:** Conceived the problem. **Baidurya Bhattacharya:** Conceived the problem.

Declaration of competing interest

The authors declare that they have no known competing financial interests or personal relationships that could have appeared to influence the work reported in this paper.

Data availability

Data will be made available on request

Acknowledgments

Appendix A. Supplementary data

Supplementary material related to this article can be found online at https://doi.org/10.1016/j.mtcomm.2023.106223.

References

[1] M.R. Khan, T.F. Rizvi, Application of nanofertilizer and nanopesticides for improvements in crop production and protection, in: Nanoscience and Plant–Soil Systems, Springer, 2017, pp. 405–427.

[2] Y. Pan, M.E. Fleet, Compositions of the apatite-group minerals: Substitution mechanisms and controlling factors, Rev. Mineral. Geochem. 48 (1) (2002) 13–49.

[3] D. MacDonald, F. Betts, S. Doty, A. Boskey, A methodological study for the analysis of apatite-coated dental implants retrieved from humans, Ann. Periodontol. 5 (1) (2000) 175–184.

[4] R. Geesink, K. de Groot, C. Klein, Bonding of bone to apatite-coated implants, J Bone Joint Surg [Br] 70 (1) (1988) 17–22.

[5] E. Landi, S. Riccobelli, N. Sangiorgi, A. Sanson, F. Doghieri, F. Miccio, Porous apatites as novel high temperature sorbents for carbon dioxide, Chem. Eng. J. 254 (2014) 586–596.

[6] A. Knox, D. Kaplan, D. Adriano, T. Hinton, M. Wilson, Apatite and phillipsite as sequestering agents for metals and radionuclides, J. Environ. Qual. 32 (2) (2003) 515–525.

[7] A.N. Amenaghawon, C.L. Anyalewechi, H. Darmokoesoemo, H.S. Kusuma, Hydroxyapatite-based adsorbents: Applications in sequestering heavy metals and dyes, J. Environ. Manag. 302 (2022) 113989.

[8] M.J. Rigali, P.V. Brady, R.C. Moore, Radionuclide removal by apatite, Am. Mineral. 101 (12) (2016) 2611–2619.

[9] V. Spallina, P. Nocerino, M.C. Romano, M. van Sint Annaland, S. Campanari, F. Gallucci, Integration of solid oxide fuel cell (SOFC) and chemical looping combustion (CLC) for ultra-high efficiency power generation and Co_2 production, Int. J. Greenh. Gas Control 71 (2018) 9–19.

[10] A. Palke, Ceramic Materials for Long-Term Sequestration of Radioactive Waste, 2011.

[11] R. Gilmore, J. Katz, Elastic properties of apatites, J. Mater. Sci. 17 (4) (1982) 1131–1141.

[12] J.D. Currey, The relationship between the stiffness and the mineral content of bone, J. Biomech. 2 (4) (1969) 477–480.

[13] E. García-Tuñón, R. Couceiro, J. Franco, E. Saiz, F. Guitián, Synthesis and characterisation of large chlorapatite single-crystals with controlled morphology and surface roughness, J. Mater. Sci., Mater. Med. 23 (10) (2012) 2471–2482.

[14] Determining the Mechanical Property of Martian Rocks Using Accurate Grain-Based Model, All Days of U.S. Rock Mechanics/Geomechanics Symposium, aRMA-2022-0508.

[15] J. Bhimasenachar, Elastic constants of apatite, Proc. Indian Acad. Sci. A 22 (1945) 209–214.

[16] H.S. Yoon, R. Newnham, Elastic properties of fluorapatite, Am. Mineral. J. Earth Planet. Mater. 54 (7–8) (1969) 1193–1197.

[17] M.C. Sha, Z. Li, R.C. Bradt, Single-crystal elastic constants of fluorapatite, Ca_5F (PO_4) 3, J. Appl. Phys. 75 (12) (1994) 7784–7787.

[18] J. Katz, K. Ukraincik, On the anisotropic elastic properties of hydroxyapatite, J. Biomech. 4 (3) (1971) 221–227.

[19] W. Bonfield, C. Li, Anisotropy of nonelastic flow in bone, J. Appl. Phys. 38 (6) (1967) 2450–2455.

[20] W. Ching, P. Rulis, A. Misra, Ab initio elastic properties and tensile strength of crystalline hydroxyapatite, Acta Biomater. 5 (8) (2009) 3067–3075.

[21] A.D. Snyder, Nanoscale Deformation Mechanisms in Bulk Hexagonal Hydroxyapatite and Effect of Defects on Mechanical Properties, Northern Illinois University, 2017.

[22] N.Y. Mostafa, P.W. Brown, Computer simulation of stoichiometric hydroxyapatite: Structure and substitutions, J. Phys. Chem. Solids 68 (3) (2007) 431–437.

[23] N.H. de Leeuw, A computer modelling study of the uptake and segregation of fluoride ions at the hydrated hydroxyapatite (0001) surface: Introducing a ca 10 (po 4) 6 (oh) 2 potential model, Phys. Chem. Chem. Phys. 6 (8) (2004) 1860–1866.

[24] E. Menendez-Proupin, S. Cervantes-Rodríguez, R. Osorio-Pulgar, M. Franco-Cisterna, H. Camacho-Montes, M. Fuentes, Computer simulation of elastic constants of hydroxyapatite and fluorapatite, J. Mech. Behav. Biomed. Mater. 4 (7) (2011) 1011–1020.

[25] N.H. de Leeuw, J.R. Bowe, J.A. Rabone, A computational investigation of stoichiometric and calcium-deficient oxy-and hydroxy-apatites, Faraday Discuss. 134 (2007) 195–214.

[26] C.-X. Li, Y.-H. Duan, W.-C. Hu, Electronic structure, elastic anisotropy, thermal conductivity and optical properties of calcium apatite Ca_5 (PO_4) 3X (X = F, Cl or Br), J. Alloys Compd. 619 (2015) 66–77.

[27] J.A.L. Rabone, N. De Leeuw, Interatomic potential models for natural apatite crystals: Incorporating strontium and the lanthanides, J. Comput. Chem. 27 (2) (2006) 253–266.

[28] Y. Suetsugu, J. Tanaka, Crystal growth and structure analysis of twin-free monoclinic hydroxyapatite, J. Mater. Sci., Mater. Med. 13 (8) (2002) 767–772.

[29] P. Alberius-Henning, E. Adolfsson, J. Grins, A. Fitch, Triclinic oxy-hydroxyapatite, J. Mater. Sci. 36 (3) (2001) 663–668.

[30] J.M. Hughes, M. Cameron, K.D. Crowley, Structural variations in natural F, OH, and Cl apatites, Am. Mineral. 74 (7–8) (1989) 870–876.

[31] R. Hill, The elastic behaviour of a crystalline aggregate, Proc. Phys. Soc. Sect. A 65 (5) (1952) 349.

[32] W. Voigt, Ueber die beziehung zwischen den beiden elasticitätsconstanten isotroper körper, Ann. Phys. 274 (12) (1889) 573–587.

[33] A. Reuß, Berechnung der fließgrenze von mischkristallen auf grund der plastizitätsbedingung für einkristalle., ZAMM J. Appl. Math. Mech. 9 (1) (1929) 49–58.

[34] P. Giannozzi, S. Baroni, N. Bonini, M. Calandra, R. Car, C. Cavazzoni, D. Ceresoli, G.L. Chiarotti, M. Cococcioni, I. Dabo, et al., Quantum espresso: A modular and open-source software project for quantum simulations of materials, J. Phys.: Condens. Matter 21 (39) (2009) 395502.

[35] J. Kohanoff, Electronic Structure Calculations for Solids and Molecules: Theory and Computational Methods, Cambridge University Press, 2006.

[36] Y. Zhang, W. Yang, Comment on generalized gradient approximation made simple, Phys. Rev. Lett. 80 (4) (1998) 890.

[37] B. Hammer, L.B. Hansen, J.K. Nørskov, Improved adsorption energetics within density-functional theory using revised Perdew–Burke–Ernzerhof functionals, Phys. Rev. B 59 (11) (1999) 7413.

[38] F. Tran, R. Laskowski, P. Blaha, K. Schwarz, Performance on molecules, and surfaces, and solids of the Wu–Cohen GGA exchange–correlation energy functional, Phys. Rev. B 75 (11) (2007) 115131.

[39] J.P. Perdew, A. Ruzsinszky, G.I. Csonka, O.A. Vydrov, G.E. Scuseria, L.A. Constantin, X. Zhou, K. Burke, Restoring the density-gradient expansion for exchange in solids and surfaces, Phys. Rev. Lett. 100 (13) (2008) 136406.

[40] J.P. Perdew, K. Burke, M. Ernzerhof, Generalized gradient approximation made simple, Phys. Rev. Lett. 77 (18) (1996) 3865.

[41] D. Vanderbilt, Soft self-consistent pseudopotentials in a generalized eigenvalue formalism, Phys. Rev. B 41 (11) (1990) 7892.

[42] H. Li, D. Wu, J. Wu, L.-Y. Dong, Y.-J. Zhu, X. Hu, Flexible, high-wettability and fire-resistant separators based on hydroxyapatite nanowires for advanced lithium-ion batteries, Adv. Mater. 29 (44) (2017) 1703548.

[43] S. Hauptmann, H. Dufner, J. Brickmann, S.M. Kast, R.S. Berry, Potential energy function for apatites, Phys. Chem. Chem. Phys. 5 (3) (2003) 635–639.

[44] A. Roy, P.K. Patra, B. Bhattacharya, Numerical estimation of elastic constants of hydroxyapatite at finite temperatures: A comparison of different force fields, in: S. Sarkar (Ed.), 7th International Congress on Computational Mechanics and Simulations, 2022, (accepted).

[45] W.G. Hoover, Canonical dynamics: Equilibrium phase-space distributions, Phys. Rev. A 31 (3) (1985) 1695.

[46] M. Catti, A. Pavese, V. Saunders, Elastic constants and electronic structure of fluorite (CaF2): An ab initio hartree-fock study, J. Phys.: Condens. Matter 3 (23) (1991) 4151.

[47] D. Pettifor, Theoretical predictions of structure and related properties of intermetallics, Mater. Sci. Technol. 8 (4) (1992) 345–349.

[48] S. Pugh, Xcii, Relations between the elastic moduli and the plastic properties of polycrystalline pure metals, Lond. Edinb. Dublin Philos. Mag. J. Sci. 45 (367) (1954) 823–843.

[49] V.V. Skripnyak, V.A. Skripnyak, et al., Predicting the mechanical properties of ultra-high temperature ceramics, Lett. Mater. 7 (2017).

[50] V.N. Staroverov, G.E. Scuseria, J. Tao, J.P. Perdew, Tests of a ladder of density functionals for bulk solids and surfaces, Phys. Rev. B 69 (2004) 075102, http://dx.doi.org/10.1103/PhysRevB.69.075102.

[51] P. Haas, F. Tran, P. Blaha, Calculation of the lattice constant of solids with semilocal functionals, Phys. Rev. B 79 (2009) 085104, http://dx.doi.org/10.1103/PhysRevB.79.085104.

[52] G.I. Csonka, J.P. Perdew, A. Ruzsinszky, P.H.T. Philipsen, S. Lebègue, J. Paier amd O.A. Vydrov, J.G. Ángyán, Assessing the performance of recent density functionals for bulk solids, Phys. Rev. B 79 (2009) 155107, http://dx.doi.org/10.1103/PhysRevB.79.155107.

[53] L. Schimka, J. Harl, G. Kresse, Improved hybrid functional for solids: The hsesol functional, J. Chem. Phys. 134 (2) (2011) 024116.

[54] J. Sun, M. Marsman, G.I. Csonka, A. Ruzsinszky, P. Hao, Y.-S. Kim, G. Kresse, J.P. Perdew, Self-consistent meta-generalized gradient approximation within the projector-augmented-wave method, Phys. Rev. B 84 (2011) 035117, http://dx.doi.org/10.1103/PhysRevB.84.035117.